



Controlled coupling of NV defect centers to plasmonic and photonic nanostructures

Michael Barth*, Stefan Schietinger, Tim Schröder, Thomas Aichele, Oliver Benson

Institute of Physics, Humboldt-Universität zu Berlin, Hausvogteiplatz 5-7, D-10117 Berlin, Germany

ARTICLE INFO

Available online 21 December 2009

Keywords:

Defect centers
Diamond
Plasmonic nanoparticles
Microsphere resonators
Photonic crystal cavities

ABSTRACT

Nitrogen-vacancy (NV) defect centers in diamond have recently emerged as promising candidates for a number of applications in the fields of quantum optics and quantum information, such as single photon generation and spin qubit operations. The performance of these defect centers can strongly be enhanced through coupling to plasmonic and photonic nanostructures, such as metal particles and optical microcavities. Here, we demonstrate the controlled assembly of such hybrid structures via manipulation with scanning near-field probes. In particular, we investigate the plasmonic enhancement of the single photon emission through coupling to gold nanospheres as well as the coupling of diamond nanocrystals to the optical modes of microsphere resonators and photonic crystal cavities. These systems represent prototypes of fundamental nanophotonic/plasmonic elements and provide control on the generation and coherent transfer of photons on the level of a single quantum emitter.

© 2009 Elsevier B.V. All rights reserved.

1. Introduction

Due to their unique optical properties, nitrogen-vacancy (NV) defect centers in diamond are appealing candidates for the realization of solid-state devices for optical quantum information processing [1,2]. Their excellent photostability [3] and ultralong spin coherence times [4] have been exploited in a number of experiments demonstrating single photon generation even at room temperature [5,6], coherent population trapping [7], and optical readout and manipulation of single nuclear spins [8–10]. In order to utilize these properties for quantum information applications and to further enhance the performance of NV centers, optical coupling to appropriate plasmonic or photonic structures (such as cavities or waveguides) [11,12] is necessary, e.g., to provide control on the generation and coherent transfer of photons in these systems. Here, we will review recent efforts on achieving such a coupling in a well-controlled fashion.

In general, two different mechanisms can be exploited to manipulate and control the optical properties of NV centers, namely the coupling to surface plasmons [13] (e.g., in metal nanostructures) or the coupling to the modes of optical microcavities or waveguides [14]. Both approaches can, in principle, be used to enhance the photon excitation and/or emission rate, to achieve strong coupling between the zero phonon transition and the photon field, and to facilitate an efficient transfer of photons from/to the NV center. Some of the optical characteristics of single

NV centers are summarized in Fig. 1, which show a typical fluorescence spectrum (Fig. 1(a)) and the normalized autocorrelation function $g^{(2)}(\tau)$ measured by a Hanbury-Brown and Twiss (HBT) setup (Fig. 1(b)).

Plasmonic nanostructures can act as optical nanoantennas, leading to highly localized photon fields and therefore to a broadband enhancement of the excitation as well as of the radiative and non-radiative decay rates of nearby emitters [15–18]. An interesting aspect is also that photons can be converted into surface plasmon polaritons, guided along plasmonic waveguide structures, and be converted back into photons [19,20]. In order to establish such a photon–plasmon interface with NV centers, a precise positioning of the NV center with respect to the plasmonic nanostructure is necessary. We tackle this problem by using nanomanipulation techniques [21,22] to gain control on the mutual position and coupling of both constituents, as will be described in detail in Section 2 [23].

Contrary to the broadband field enhancement present in plasmonic structures, optical microcavities provide spectrally narrow resonances with high Q-factors. Combined with small modal volumes, these resonances are well suited to achieve a coherent coupling between the zero phonon transition and the optical mode [11], which is required for the observation of cavity quantum electrodynamic (QED) effects and the realization of interfaces between stationary and flying qubits in quantum information processing devices [2]. In principle, an appropriate microcavity can directly be realized in diamond [24,25], but first experimental demonstrations with microdisk resonators [26] and photonic crystal (PC) cavities [27] suffered from large absorption and scattering losses owing to the poly-crystallinity of the

* Corresponding author. Tel.: +49 30 2093 4941; fax: +49 30 2093 4718.
E-mail address: michael.barth@physik.hu-berlin.de (M. Barth).

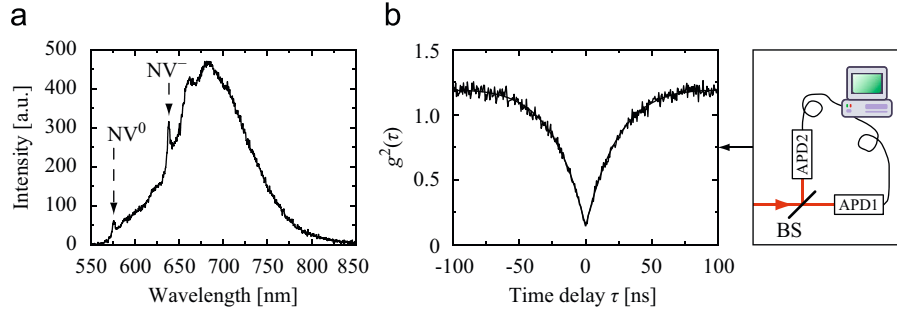


Fig. 1. (a) Typical fluorescence spectrum of a single NV center in a diamond nanocrystal at room temperature. Two zero phonon lines can be observed, associated with the neutral (NV^0) and negatively charged (NV^-) state of the NV center. (b) Second order correlation function $g^{(2)}(\tau)$ (left) of the same NV center, measured using an HBT setup (right). The dip at $\tau=0$ clearly indicates the single photon character of the emission. The HBT setup consists of a beamsplitter (BS) and two avalanche photodiodes (APDs).

employed diamond material. Corresponding implementations with single-crystalline diamond [28] are very challenging and have not yet been realized. An alternative approach is the use of resonators made from non-diamond material to which NV centers are coupled. Such hybrid devices can either incorporate single-crystalline diamond films [29–31] or diamond nanocrystals [32–34]. Using bulk diamond has the advantage of superior optical properties of the NV centers, as nanocrystals can induce inhomogeneous broadening and spectral diffusion of the zero photon transition [35]. However, coupling of a single NV center in such a structure has not yet been demonstrated. In our studies we use diamond nanocrystals containing single NV centers. Again, we exploit nanomanipulation techniques to demonstrate the controlled coupling to microsphere resonators [36,37], as described in Section 3.1, and to PC cavities [38,39], as described in Section 3.2.

2. Coupling of NV centers to plasmonic nanoparticles

In this section we review the experimental realization of a controlled coupling between diamond nanocrystals (20–35 nm in height, purchased from Microdiamant) and spherical gold nanoparticles (60 nm in diameter, purchased from BBInternational) through manipulation with an atomic force microscope (AFM) [23]. The corresponding experimental setup is shown in Fig. 2(a). A homemade inverted confocal microscope allows us to simultaneously perform optical measurements and nanoscale manipulation on particles. For excitation we use a frequency-doubled Nd:YAG laser ($\lambda_{\text{exc}}=532$ nm) and a frequency-doubled, picosecond-pulsed amplified diode laser ($\lambda_{\text{exc}}=531$ nm, 100 ps pulse width, 2.5 MHz repetition rate) allowing continuous wave and pulsed excitation, respectively. The polarization direction of the excitation light is controlled by a $\lambda/2$ waveplate. An oil immersion objective ($60\times/1.4$ NA) is used for focusing the excitation light onto the sample and for collection of the fluorescence emission. After passing a 550 nm longpass filter and a 50 μm pinhole, the fluorescence light can either be monitored by a CCD camera, spectrally dispersed and imaged by a spectrograph, or it can be analyzed in an HBT correlator (see inset in Fig. 1(b)). An AFM in tapping mode is used for mapping the topography of the sample, while manipulation of the particles is performed in contact mode. In a preliminary step the sample is prepared by spin-coating an aqueous solution of diamond nanocrystals and gold nanoparticles onto a glass coverslip. Approximately 1% of the nanodiamonds contain a single NV center, as determined by comparing AFM measurements with corresponding confocal scans of the sample and analyzing the $g^{(2)}(\tau)$ function of the fluorescence from individual nanocrystals. These nanocrystals are then selected for subsequent experiments.

The assembly of the hybrid structure is performed by maneuvering gold nanoparticles to a particular diamond nanocrystal via AFM manipulation and bringing all constituents into direct contact. In Fig. 2(b) two specific configurations are shown, namely a nanodiamond with one gold sphere attached (denoted as configuration A) and the same nanodiamond sandwiched between two gold spheres (denoted as configuration B). Three-dimensional finite-difference time-domain calculations are performed to estimate the plasmonic enhancement effects in these configurations (Fig. 2(c)). Thereby, the diamond nanocrystal is modeled as a truncated four-sided pyramid. Realistic material parameters are used and the influence of the glass substrate as well as the excitation with a high-NA objective is taken into account. Simulations of the excitation field predict a strong field enhancement only for polarizations along the x axis. In this case, pronounced hot spots are formed at the contact points between the diamond and gold particles, giving rise to an enhanced electric field inside the diamond nanocrystal, even if the latter is considerably smaller than the gold spheres. This effect leads to an enhancement of the excitation as well as emission rate of the NV center, provided that the dipole moment of the latter has a significant component in x direction.

From time-resolved measurements (Fig. 3(a)) on the configurations A (blue) and B (red) we obtain an increase in the excited-state decay rate $1/\tau_{\text{dec}}$ by a factor of 7.5 and 9.5, respectively. To check whether this enhancement is due to radiative or non-radiative processes, power-dependent measurements were performed (Fig. 3(b)). The data was fitted with a saturation model [40] of the form $P=\xi\sigma\Phi I_{\text{exc}}/(1+\sigma\Phi\tau_{\text{rad}}I_{\text{exc}})$, where σ is the absorption cross section, τ_{rad} is the radiative lifetime, Φ is the internal quantum efficiency, I_{exc} is the excitation intensity, and ξ is the total collection efficiency of our setup. Under strong excitation, the maximum number of emitted photons is only restricted by the radiative lifetime and the formula reduces to $P=\xi/\tau_{\text{rad}}$. Since our simulations show only a negligible influence of the gold spheres on the collection efficiency, we assume ξ to be constant and can thus deduce an increase in the radiative decay rate $1/\tau_{\text{rad}}$ by a factor of 5.8 and 8.9 for configurations A and B, respectively. This corresponds to quantum efficiencies $\Phi=\tau_{\text{dec}}/\tau_{\text{rad}}$ of 0.78 and 0.93, when $\Phi=0.99$ is assumed for the bare nanodiamond [41]. Obviously, in our configuration the first gold sphere induces a noticeable non-radiative decay channel (thus reducing the quantum efficiency), while the second gold sphere predominantly enhances the radiative decay rate (thus partly restoring the original quantum efficiency). This can be attributed to different distances of the gold spheres to the NV center and thus to a different impact of fluorescence quenching effects [16,17]. Note that the enhancement of the radiative decay rate by nearly an order of magnitude is, to our knowledge, so far the highest achieved for NV centers in

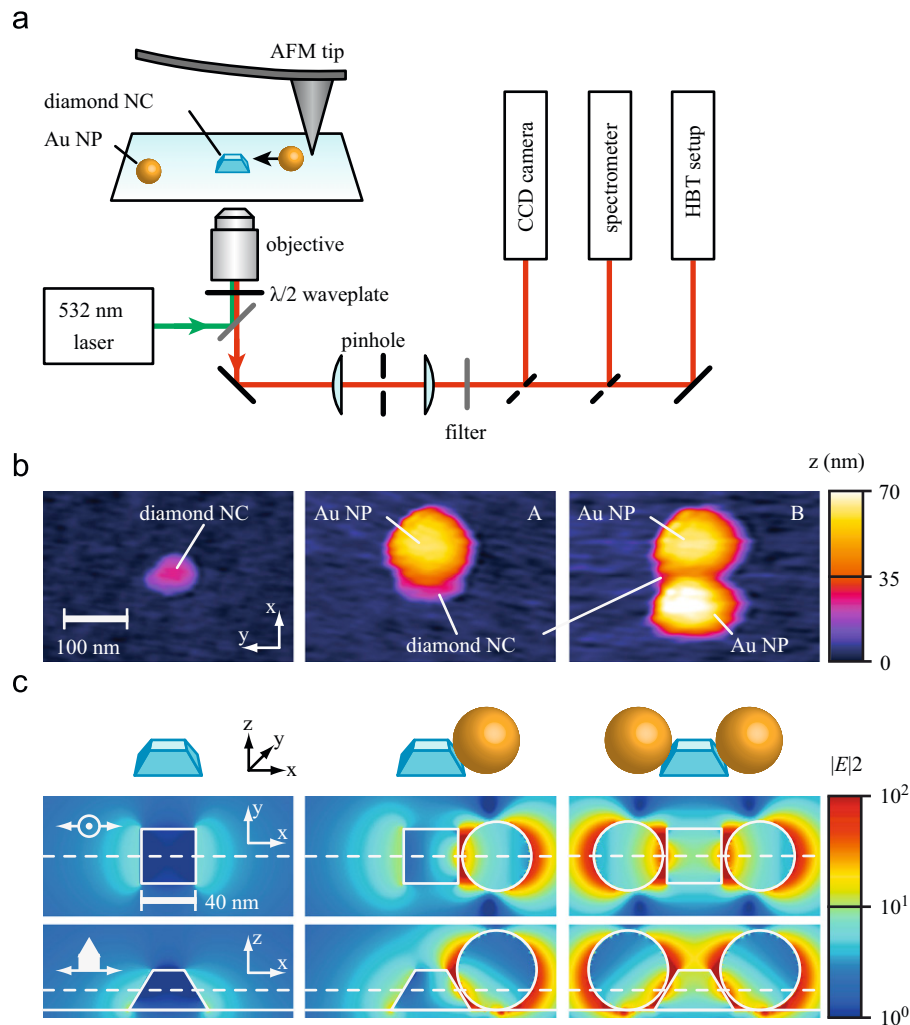


Fig. 2. (a) Experimental setup for simultaneous optical detection and manipulation of diamond nanocrystals (NCs) and gold nanoparticles (NPs). (b) AFM images of various diamond–gold configurations. (c) Corresponding numerical simulations for light of wavelength $\lambda = 532$ nm, impinging from below and polarized along the x direction. The electric field intensity is normalized to the value at the center of the bare nanodiamond and displayed in a logarithmic color scale.

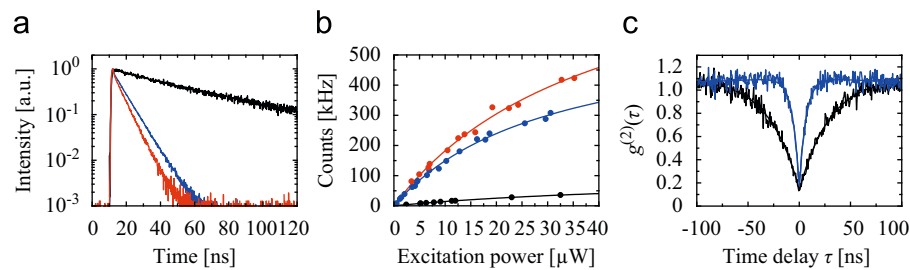


Fig. 3. (a) Fluorescence timetraces of the bare diamond (black), configuration A (blue) and configuration B (red). (b) Corresponding measurements of the detected intensity as a function of the excitation power. (c) Autocorrelation measurement from configuration A (blue) in comparison to the bare nanodiamond (black). Configuration B shows similar results, which have been omitted for clarity. (For interpretation of the references to colour in this figure legend, the reader is referred to the web version of this article.)

diamond and is equivalent to an increase in the maximum single photon rate by the same factor.

Under weak excitation the above formula reduces to $P = \xi \sigma \Phi I_{\text{exc}}$ and allows us to extract the enhancement of the excitation rate $\gamma_{\text{exc}} = \sigma I_{\text{exc}}$ from the slope of the power-dependent measurements in Fig. 3(b) at low excitation power. A 12- and 14-fold enhancement can be deduced for configurations A and B, respectively. This is the overall enhancement of γ_{exc} and stems from an enhanced I_{exc} due to local field effects as well as a higher

σ because of plasmonic amplification of the excitation transition. Again, the effect of the second gold sphere is not as pronounced as that of the first one, supposedly due to the non-central location of the NV center inside the nanodiamond and thus different distances to the gold particles.

While both, the excitation and emission rate are strongly enhanced, the single photon character of the emission is still preserved, as can be seen from corresponding measurements of the second order autocorrelation function $g^{(2)}(\tau)$ (Fig. 3(c)).

Consequently, plasmonic nanostructures can be employed to improve the single photon generation of individual NV centers over a broad spectral range, or to efficiently convert the optical excitation energy into single propagating surface plasmon polaritons [19,20].

3. Coupling of NV centers to optical microcavities

While plasmonic nanostructures provide a broadband enhancement of the transition rates of NV centers, optical microcavities promise coherent coupling of the emission from the Fourier limited zero phonon line to a single resonant mode [11]. Such a coupling scheme is beneficial for the creation of single photon sources with a high degree of photon indistinguishability. The latter is crucial, e.g., for establishing “single photon nonlinearities” in Hong-Ou-Mandel type experiments [42]. Prerequisites for a strong coupling between an NV center and a particular mode of an optical microcavity are a high Q -factor and a small mode volume. Here, we review two recent efforts to establish such a coupling using microsphere resonators (Section 3.1) and PC cavities (Section 3.2).

3.1. Coupling to microsphere resonators

The first approach is to couple individual NV centers to polystyrene (PS) microspheres acting as resonators. In such dielectric spheres light can be trapped close to the inner surface due to total internal reflection. Modes with tightest confinement of light are the so-called whispering gallery modes (WGMs), which provide high quality factors and small mode volumes [43]. Both are necessary to observe cavity QED effects [44]. In addition, it has been shown that microsphere resonators can be implemented as building blocks for more complex nanophotonic devices, e.g., in coupled resonator optical waveguides [45] or energy transfer systems [46]. The main advantage of the approach presented in the following is that the individual quantum emitters and cavities can be pre-characterized in a first step before they are assembled. Therefore, rather elaborate post-selection [47,48] or tuning schemes [49,50] can be circumvented in future experiments.

The experimental setup (Fig. 4(a)) is similar to the one shown in Fig. 2(a), but the AFM is replaced by a homebuilt, shear-force controlled scanning near-field optical microscope (SNOM) as the tip of the SNOM is more suitable to manipulate the micrometer-

sized PS spheres. To avoid strong Raman background from the PS, the 514 nm laser line of an argon ion laser is used for the excitation of the NV centers instead of the 532 nm laser in Fig. 2(a). The experimental procedure starts with the preparation of the sample by spin coating nanodiamonds and drop casting an isopropanol suspension of PS spheres ($\sim 4.8 \mu\text{m}$ in diameter) on a coverslip. By white light illumination the microspheres can easily be monitored on the CCD camera in the microscope setup. One of the spheres is chosen and attached to the SNOM probe by bringing the glass tip in full contact with the sphere. After retracting the SNOM probe with the attached PS sphere, a single NV center is located and characterized with the help of the spectrometer and an HBT correlator. The sphere is lowered (Fig. 4(b)) and positioned directly above a single nanodiamond (Fig. 4(c)) with the help of simultaneous excitation of the NV center and white light illumination from above. Prior to the manipulation it has been verified that the nanocrystal contains only a single NV center by inspecting the corresponding $g^{(2)}(\tau)$ function. By further lowering the sphere into full contact with the sample and moving it across the surface, the nanodiamond can be attached to the microsphere. The coupled system can be retracted and it is possible to move the sample underneath as shown in Fig. 4(d) and (e). After elevating and re-adjusting the focus, the spectrum and the $g^{(2)}(\tau)$ function are recorded with an additional 630 nm longpass filter to block emission coming from the PS sphere itself. The spectrum (Fig. 4(f)) shows pronounced resonances as the fluorescence couples to the WGMs of the microsphere with Q -factors of up to 5500. At the same time the $g^{(2)}(\tau)$ function exhibits an antibunching dip well below 0.5 at $\tau=0$, proving that indeed a single quantum emitter is coupled to the microsphere resonator. By comparison with Mie theory one can derive the radius of the sphere to be $2.45 \mu\text{m}$ and assign the individual resonances, as indicated in Fig. 5(a).

A major improvement of our method is the possibility to preselect the resonator by choosing an appropriate microsphere. In order to characterize the mode spectrum of individual spheres before the coupling to the NV center, the sample is illuminated with white light from the side. The scattered light is collected by the objective in the confocal setup and an appropriate spatial position on the sample is filtered out by the confocal pinhole before entering the spectrometer. The scattering spectrum of a sphere is shown in Fig. 5(a) (red curve). The slightly asymmetric shape of the resonances stems from interference with so-called van de Hulst surface waves [51], which can be observed under certain detection angles. By comparison of this spectrum to the calculated one resulting from Mie theory [52], it is obvious that modes with

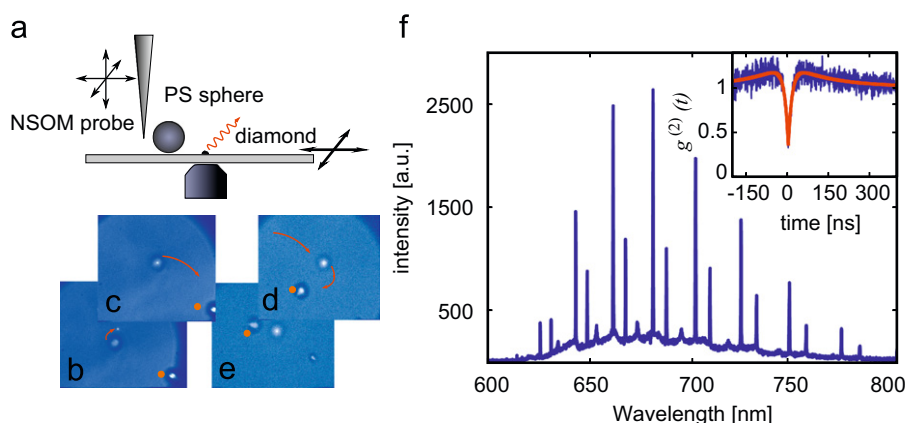


Fig. 4. (a) Setup: instead of the AFM a SNOM probe is used for manipulation. (b)–(e) Picking-up of the nanodiamond: the sphere is positioned right above the nanodiamond and brought into full contact. The coupled system is lifted and the sample can be moved underneath. The red spot marks the same position in each picture. (f) The spectrum of the nanodiamond attached to the sphere exhibits strong modulation because of the coupling to the WGMs, while the anti-bunching dip stays below 0.5 (inset). (For interpretation of the references to colour in this figure legend, the reader is referred to the web version of this article.)

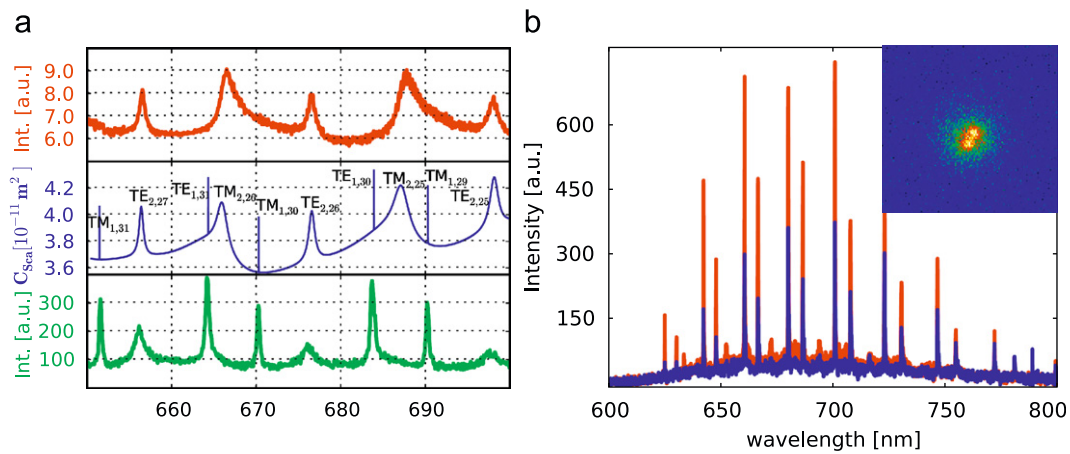


Fig. 5. (a) White light scattering spectrum of a bare sphere (red), spectrum fitted with Mie-theory (blue), and spectrum emitted by the nanodiamond attached to the sphere (green). Good agreement for the calculated and measured spectral position of the high- Q WGMs with an accuracy of 0.2 nm can be achieved. (b) Two single NV centers attached to a sphere (inset), both sharing the same WGMs. (For interpretation of the references to colour in this figure legend, the reader is referred to the web version of this article.)

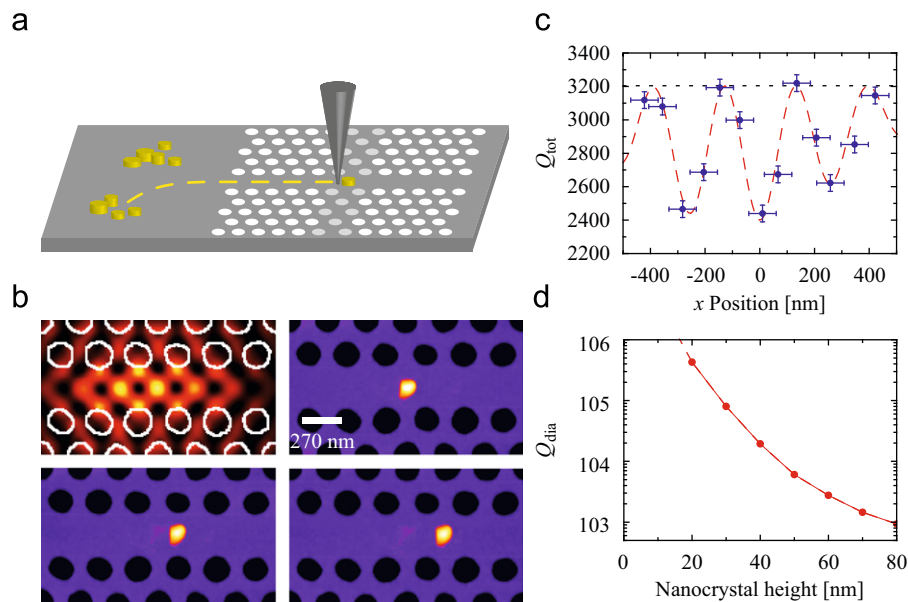


Fig. 6. (a) Schematic illustration of the heterostructure cavity and the particle positioning via an AFM tip. (b) AFM images of different diamond-cavity configurations as well as the calculated mode profile (upper left panel) of the fundamental cavity mode. (c) Measured (blue) and theoretically estimated (red) Q -factors of the fundamental cavity mode as a function of the nanodiamond position. The dotted line indicates the Q -factor of the bare cavity. (d) Calculated impact of nanodiamonds of different size, placed above the center of the cavity, on the cavity Q -factor. (For interpretation of the references to colour in this figure legend, the reader is referred to the web version of this article.)

highest Q do not occur in the scattered spectrum. The explanation for this can be found by introducing additional losses in the Mie theory, which results in an overall reduction of the scattered intensity of the highest Q modes by a factor of 30, making them undetectable in the scattered spectrum. Nevertheless, it is possible to calculate the exact spectral position of all resonances by fitting the calculated Mie spectrum to the experimental one using the sphere radius as fitting parameter. The fitted spectrum and the emission of an attached single NV center can also be found in Fig. 5(a) (blue and green curve, respectively). It turns out that the pre-characterization can predict the high Q modes with an accuracy of 0.2 nm, which is mainly limited by the resolution and spectral accuracy of the spectrometer.

The procedure of coupling individual quantum emitters to microspheres is not restricted to single emitters and single microspheres. For example, after attaching a first nanodiamond, the coupled system can be retracted and a second nanodiamond

can be located. Fig. 5(b) shows the spectra of two single emitters attached to the same microsphere next to each other (see inset). The positions of the resonances match within the resolution of the spectrometer, demonstrating that we are able to couple quantum emitters to shared modes of a microresonator on demand.

3.2. Coupling to photonic crystal cavities

The second approach is to couple individual NV centers to planar PC cavities made from silicon nitride (refractive index $n=2.01$), which can operate in a broad region of the visible spectrum, including the relevant emission band of NV centers. In particular, we use a double-heterostructure cavity (formed by a locally modulated PC waveguide) [53,54] with a Q -factor of approximately 3200, small modal volume $\sim 2 (\lambda/n)^3$, and a resonance wavelength near 650 nm. A schematic illustration of

the cavity design is shown in Fig. 6(a) and details on its fabrication can be found in Ref. [54]. For our approach, the main advantage of the modulated waveguide design lies in the direct connection of the cavity (via the waveguide) to a region outside the PC array, where reservoirs of nanodiamonds can be deposited (see cartoon in Fig. 6(a)). In this way, nanodiamonds can be moved in and out of the cavity (along the waveguide) using the cantilever tip of the AFM, similar to the procedure described in Section 2. In detail, the deposition scheme works as follows. First, a tapered silica fiber (tip radius $\sim 1\ \mu\text{m}$) is dipped into an aqueous solution of diamond nanocrystals (20–200 nm size distribution) and brought into contact with a sample region next to the PC array. This so-called dip-pen technique [55] creates small reservoirs of nanodiamonds on the sample surface. Next, these reservoirs are imaged with the AFM and nanodiamonds of appropriate size and shape can be selected and maneuvered into the cavity (see Fig. 6(a)).

The optical properties of this combined diamond-cavity system are studied using a scanning confocal optical microscope setup similar to the one shown in Fig. 2(a), with the major difference that a $100\times/0.9$ NA microscope objective is used to excite and collect fluorescence from the top of the PC sample, since the latter is opaque. As only a few percent of the nanodiamonds employed here actually contain NV centers, most of the deposited nanocrystals do not show any fluorescence. However, even in the absence of an NV center the optical properties of the diamond-cavity system can be investigated by monitoring the intrinsic fluorescence signal from the silicon nitride membrane itself. It should be noted that this intrinsic emission, while being useful for characterization, is also the main drawback of the employed cavities as it adds a considerable background signal to the single photon emission of the NV centers. This problem may be tackled in future studies by using other cavity materials such as GaP.

The main results of one particular experiment are depicted in Fig. 6(b) and (c). A relatively large nanodiamond (55 nm in height, 50–100 nm lateral dimensions) was chosen to achieve a noticeable impact on the optical properties of the PC cavity. Note that this particular nanodiamond did not contain any NV centers. AFM images of some of the assembled diamond-cavity configurations are shown in Fig. 6(b). The orientation of the nanodiamond (discernible from its asymmetric shape) is kept constant in all configurations to ensure consistency between measurements. Theoretical studies of these configurations were performed by deducing the real geometry of the cavity as well as that of the nanodiamond from the AFM images and adopting it in three-dimensional FDTD simulations. The corresponding calculated electric field intensity distribution (without any diamond nanocrystal) is also displayed in Fig. 6(b). It clearly shows an asymmetry in the mode pattern due to slight fabrication imperfections. The experimental values of the total Q -factor Q_{tot} of the combined diamond-cavity system are determined from the recorded fluorescence spectra as a function of the position of the nanodiamond with respect to the center ($x=0$) of the cavity. The results are shown in Fig. 6(c). The corresponding theoretical results (for the real cavity structure) are scaled such that the simulated value $Q_0=4800$ of the bare cavity matches the experimental value $Q=3200$ and are also displayed in Fig. 6(c) (dashed curve) for comparison. The scaling is justified because not all imperfections (such as surface roughness) leading to a degradation of Q can be accounted for in the simulation. Excellent agreement between experiment and theory is achieved. Clearly, the influence of the nanodiamond on the Q -factor coincides with the intensity distribution of the cavity mode. Even the asymmetric mode profile found in the simulation is reproduced in the experimental data.

While this rather large diamond nanocrystal has a strong impact on the cavity properties when placed in a field antinode, the question arises whether smaller nanodiamonds can be coupled without disturbing the Q -factor significantly. For this purpose FDTD simulations with nanodiamonds of different sizes, placed upon the center of the cavity, were performed. The corresponding Q -factors Q_{dia} , (representing the contribution of the diamond nanocrystal to the total Q -factor Q_{tot} according to the formula $1/Q_{\text{tot}}=1/Q_0+1/Q_{\text{dia}}$) are shown in Fig. 6(d). As is evident, nanodiamonds with dimensions smaller than 20 nm are well suited for cavity QED experiments as they still allow the realization of combined diamond-cavity systems with quality factors $Q_{\text{tot}} > 10^5$.

4. Conclusions

In conclusion, we have demonstrated the controlled coupling of individual NV defect centers in diamond to plasmonic and photonic nanostructures, thereby manipulating and enhancing the optical properties of the NV centers. These hybrid systems represent prototypes of fundamental building blocks for the realization of integrated optical devices, e.g., for quantum information processing. Although their assembly via nanomanipulation is demanding and often time-consuming, recent advances in handling and positioning individual diamond nanocrystals on purpose [56,57] promise more efficient routes for creating these structures. Then, it will also be possible to establish more complex nanophotonic/plasmonic devices, incorporating coupled cavities, waveguides, and plasmonic elements in combination with multiple, well-placed defect centers in diamond.

Acknowledgement

This work was supported by the DFG (SFB 448 and BE 2224/9).

References

- [1] J. Wrachtrup, F. Jelezko, *J. Phys. Cond. Matter* 18 (2006) S807.
- [2] S. Praver, A.D. Greentree, *Science* 320 (2008) 1601.
- [3] F. Jelezko, J. Wrachtrup, *Phys. Status Solidi A* 203 (2006) 3207.
- [4] G. Balasubramanian, P. Neumann, D. Twitchen, M. Markham, R. Kolesov, N. Mizuochi, J. Isoya, J. Achard, J. Beck, J. Tisler, V. Jacques, P.R. Hemmer, F. Jelezko, J. Wrachtrup, *Nat. Mater.* 8 (2009) 383.
- [5] C. Kurtsiefer, S. Mayer, P. Zarda, H. Weinfurter, *Phys. Rev. Lett.* 85 (2000) 290.
- [6] A. Beveratos, R. Brouri, T. Gacoin, A. Villing, J.-P. Poizat, P. Grangier, *Phys. Rev. Lett.* 89 (2002) 187901.
- [7] C. Santori, P. Tamarat, P. Neumann, J. Wrachtrup, D. Fattal, R.G. Beausoleil, J.R. Rabeau, P. Olivero, A.D. Greentree, S. Praver, F. Jelezko, P. Hemmer, *Phys. Rev. Lett.* 97 (2006) 247401.
- [8] T. Gaebel, M. Domhan, I. Popa, C. Wittmann, P. Neumann, F. Jelezko, J.R. Rabeau, N. Stavrias, A.D. Greentree, S. Praver, J. Meijer, J. Twamley, P.R. Hemmer, J. Wrachtrup, *Nat. Phys.* 2 (2006) 408.
- [9] L. Childress, M.V. Gurudev Dutt, J.M. Taylor, A.S. Zibrov, F. Jelezko, J. Wrachtrup, P.R. Hemmer, M.D. Lukin, *Science* 314 (2006) 281.
- [10] M.V. Gurudev Dutt, L. Childress, L. Jiang, E. Togan, J. Maze, F. Jelezko, A.S. Zibrov, P.R. Hemmer, M.D. Lukin, *Science* 316 (2007) 1312.
- [11] C.-H. Su, A.D. Greentree, L.C.L. Hollenberg, *Opt. Express* 16 (2008) 6240.
- [12] A. Young, C.Y. Hu, L. Marseglia, J.P. Harrison, J.L. O'Brien, J.G. Rarity, *New J. Phys.* 11 (2009) 013007.
- [13] W.L. Barnes, A. Dereux, T.W. Ebbesen, *Nature* 424 (2003) 824.
- [14] K.J. Vahala, *Nature* 424 (2003) 839.
- [15] J. Farahani, D. Pohl, H. Eisler, B. Hecht, *Phys. Rev. Lett.* 95 (2005) 17402.
- [16] P. Anger, P. Bharadwaj, L. Novotny, *Phys. Rev. Lett.* 96 (2006) 113002.
- [17] S. Kühn, U. Håkanson, L. Rogobete, V. Sandoghdar, *Phys. Rev. Lett.* 97 (2006) 17402.
- [18] T. Taminiau, F. Stefani, F. Segerink, N. van Hulst, *Nat. Photon* 2 (2008) 234.
- [19] A. Akimov, A. Mukherjee, C. Yu, D. Chang, A. Zibrov, P.R. Hemmer, H. Park, M.D. Lukin, *Nature* 450 (2007) 402.
- [20] R. Kolesov, B. Grotz, G. Balasubramanian, R.J. Stöhr, A.A.L. Nicolet, P.R. Hemmer, F. Jelezko, J. Wrachtrup, *Nat. Phys.* 5 (2009) 470.
- [21] J. Merlein, M. Kahl, A. Zuschlag, A. Sell, A. Halm, J. Boneberg, P. Leiderer, A. Leitenstorfer, R. Bratschkitsch, *Nat. Photon* 2 (2008) 230.

- [22] A. Bek, R. Jansen, M. Ringler, S. Mayilo, T. Klar, J. Feldmann, *Nano Lett.* 8 (2008) 485.
- [23] S. Schietinger, M. Barth, T. Aichele, O. Benson, *Nano Lett.* 9 (2009) 1694.
- [24] S. Tomljenovic-Hanic, M.J. Steel, C.M. de Sterke, J. Salzman, *Opt. Express* 14 (2006) 3556.
- [25] C. Kreuzer, J. Riedrich-Möller, E. Neu, C. Becher, *Opt. Express* 16 (2008) 1632.
- [26] C.F. Wang, Y.-S. Choi, J.C. Lee, E.L. Hu, J. Yang, J.E. Butler, *Appl. Phys. Lett.* 90 (2007) 081110.
- [27] C.F. Wang, R. Hanson, D.D. Awschalom, E.L. Hu, T. Feygelson, J. Yang, J.E. Butler, *Appl. Phys. Lett.* 91 (2007) 201112.
- [28] B.A. Fairchild, P. Olivero, S. Rubanov, A.D. Greentree, F. Waldermann, I.W. Robert, A. Taylor, J.M. Smith, S. Huntington, B.C. Gibson, D.N. Jamieson, S. Praver, *Adv. Mater.* 20 (2008) 4793.
- [29] K.-M. Fu, C. Santori, P.E. Barclay, I. Aharonovich, S. Praver, N. Meyer, A.M. Holm, R.G. Beausoleil, *Appl. Phys. Lett.* 93 (2008) 234107.
- [30] P.E. Barclay, K.-M. Fu, C. Santori, R.G. Beausoleil, *Opt. Express* 17 (2009) 9588.
- [31] M. Larsson, K.N. Dinyari, H. Wang, *Nano Lett.* 9 (2009) 1447.
- [32] Y.-S. Park, A.K. Cook, H. Wang, *Nano Lett.* 6 (2006) 2075.
- [33] M.W. McCutcheon, M. Lončar, *Opt. Express* 16 (2008) 19136.
- [34] P.E. Barclay, O. Painter, C. Santori, K.-M. Fu, R.G. Beausoleil, *Opt. Express* 19 (2009) 8081.
- [35] Y. Shen, T.M. Sweeney, H. Wang, *Phys. Rev. B* 77 (2008) 033201.
- [36] S. Schietinger, T. Schröder, O. Benson, *Nano Lett.* 8 (2008) 3911.
- [37] S. Schietinger, O. Benson, *J. Phys. B* 42 (2009) 114001.
- [38] M. Barth, J. Stingl, J. Kouba, N. Nüsse, B. Löchel, O. Benson, *Phys. Status Solidi B* 246 (2009) 298.
- [39] M. Barth, N. Nüsse, B. Löchel, O. Benson, *Opt. Lett.* 34 (2009) 1108.
- [40] J. Enderlein, *Chem. Phys. Lett.* 410 (2005) 452.
- [41] T. Gaebel, M. Domhan, C. Wittmann, I. Popa, F. Jelezko, J. Rabeau, A.D. Greentree, S. Praver, E. Trajkov, P. P. R. Hemmer, J. Wrachtrup, *Appl. Phys. B* 82 (2006) 243.
- [42] C.K. Hong, Z.Y. Ou, L. Mandel, *Phys. Rev. Lett.* 59 (1987) 2044.
- [43] V. Braginsky, M. Gorodetsky, V. Ilchenko, *Phys. Lett. A* 137 (1989) 393.
- [44] J. Buck, H. Kimble, *Phys. Rev. A* 67 (2003) 33806.
- [45] B. Möller, U. Woggon, M. Artemyev, *Opt. Lett.* 30 (2005) 2116.
- [46] S. Götzinger, L. Menezes, A. Mazzei, S. Kühn, V. Sandoghdar, O. Benson, *Nano Lett.* 6 (2006) 1151.
- [47] T. Yoshie, A. Scherer, J. Hendrickson, G. Khitrova, H. Gibbs, G. Rupper, C. Ell, O. Shchekin, D. Deppe, *Nature* 432 (2004) 200.
- [48] J. Michaelis, C. Hettich, J. Mlynek, V. Sandoghdar, *Nature* 405 (2000) 325.
- [49] A. Badolato, K. Hennessy, M. Atatüre, J. Dreiser, E. Hu, P. Petroff, A. Imamoglu, *Science* 308 (2005) 1158.
- [50] L. Wang, A. Rastelli, S. Kiravittaya, P. Atkinson, F. Ding, C.C. Bof Bufon, C. Hermannstädter, M. Witzany, G.J. Beirne, P. Michler, O.G. Schmidt, *New J. Phys.* 10 (2008) 045010.
- [51] A. Ashkin, J.M. Dziedzic, *Appl. Opt.* 20 (1981) 1803.
- [52] C.F. Bohren, D.R. Huffman, in: *Absorption and Scattering of Light by Small Particles*, John Wiley & Sons Inc, 1998.
- [53] B.S. Song, S. Noda, T. Asano, Y. Akahane, *Nat. Mater.* 4 (2005) 207.
- [54] M. Barth, N. Nüsse, J. Stingl, B. Löchel, O. Benson, *Appl. Phys. Lett.* 93 (2008) 021112.
- [55] M.S. Anderson, *Appl. Phys. Lett.* 92 (2008) 123101.
- [56] T. van der Sar, E.C. Heeres, G.M. Dmochowski, G. de Lange, L. Robledo, T.H. Oosterkamp, R. Hanson, *Appl. Phys. Lett.* 94 (2009) 173104.
- [57] E. Ampem-Lassen, D.A. Simpson, B.C. Gibson, S. Trpkovski, F.M. Hossain, S.T. Huntington, K. Ganesan, L.C.L. Hollenberg, S. Praver, *Opt. Express* 17 (2009) 11287.